

Key Points:

- The majority of phytoplankton production occurs during the spring bloom
- Phytoplankton growth rates appear limited by nutrient availability in late summer
- Profiling Crawlers provides new insight into the seasonal production cycle in the southeastern Bering Sea

Supporting Information:

Supporting Information may be found in the online version of this article.

Correspondence to:








J. M. Nielsen,
jens.nielsen@noaa.gov

Citation:

Nielsen, J. M., Pelland, N. A., Bell, S. W., Lomas, M. W., Eisner, L. B., Stabeno, P., et al. (2023). Seasonal dynamics of primary production in the southeastern Bering Sea assessed using continuous temporal and vertical dissolved oxygen and chlorophyll-*a* measurements. *Journal of Geophysical Research: Oceans*, 128, e2022JC019076. <https://doi.org/10.1029/2022JC019076>

Received 7 JUL 2022
Accepted 6 APR 2023

Seasonal Dynamics of Primary Production in the Southeastern Bering Sea Assessed Using Continuous Temporal and Vertical Dissolved Oxygen and Chlorophyll-*a* Measurements

Jens M. Nielsen^{1,2} , Noel A. Pelland^{1,3} , Shaun W. Bell⁴ , Michael W. Lomas⁵ , Lisa B. Eisner², Phyllis Stabeno⁴ , Colleen Harpod² , Scott Stalin⁴, and Calvin W. Mordy^{1,4} 

¹Cooperative Institute for Climate, Ocean, and Ecosystem Studies, University of Washington, Seattle, WA, USA, ²Alaska Fisheries Science Center, National Oceanic and Atmospheric Administration, Seattle, WA, USA, ³Marine Mammal Laboratory, Alaska Fisheries Science Center, National Marine Fisheries Service, Seattle, WA, USA, ⁴Pacific Marine Environmental Laboratory, NOAA, Seattle, WA, USA, ⁵Bigelow Lab for Ocean Sciences, East Boothbay, ME, USA

Abstract The Bering Sea and other high-latitude systems are experiencing unprecedented changes related to climate warming and the consequent loss of sea ice. Understanding how such changes influence primary production is a pressing question. Here, we quantify primary production rates in the southeastern Bering Sea over 4 years (2016–2019) at daily to weekly time resolution. A moored high-resolution Profiling Crawler was used in combination with in situ sampling to collect physical and biological data in the ocean's upper 50 m. We used dissolved oxygen (O₂) data to estimate gross and net primary production (NPP), and chlorophyll-*a* (Chl-*a*), temperature, and irradiance data to model NPP rates. We then assessed seasonal variation in phytoplankton production rates, phytoplankton community growth rates (p_{opt}^b) and explored to what extent summer phytoplankton community growth rates may be influenced by nitrogen limitation. Our analyses revealed that the majority of gross primary production (GPP) and net community production occurs in association with the spring phytoplankton bloom. After the bloom, the water column generally experienced low GPP and net biological carbon consumption. Phytoplankton growth rates were commonly suppressed in late summer due to apparent nitrogen depletion. Using high temporal resolution vertically resolved measurements of O₂ and Chl-*a*, our analyses provides important insight into how biogeochemical cycles, phytoplankton community growth rates, and carbon available for export vary seasonally in the southeastern Bering Sea.

Plain Language Summary The Bering Sea is experiencing unprecedented changes related to climate warming and the consequent loss of sea ice. How such changes affect the growth and composition of phytoplankton at the base of the food web is a pressing concern. Here, we quantify phytoplankton and community production rates in the surface ocean in the southeastern Bering Sea over four years (2016–2019), using a moored Profiling Crawler that samples temperature, salinity, oxygen, and chlorophyll-*a* data over the top 50 m. We then assessed seasonal and shorter-term variations in phytoplankton production rates. Our analyses showed that the majority of phytoplankton production and organic carbon available for leaving the upper ocean occurs during the phytoplankton spring bloom. After the bloom, phytoplankton production was low for most of the summer, with phytoplankton growth rates limited by nutrient availability in late summer. Our high temporal resolution and vertically resolved measurements from the Profiling Crawler provide new insight into the seasonal primary production cycle in the southeastern Bering Sea.

1. Introduction

Ocean primary production plays a major role in the global carbon cycle, accounting for about half of the world's carbon fixation (Falkowski et al., 1998). Primary production rates vary with temperature, nutrient, and light conditions (Bouman et al., 2018; Moore et al., 2013), and influence biogeochemical cycles and marine ecosystem productivity (Falkowski et al., 1998). Measures of gross primary production (GPP), net primary production (NPP), and net community production (NCP) rates, and phytoplankton community growth rates (p_{opt}^b , i.e., the normalized primary production rates relative to chlorophyll-*a*, Chl-*a*) provide key metrics for assessing the fate of energy production by phytoplankton, energy availability to heterotrophs (e.g., bacteria, zooplankton, and fish) and the amount of organic carbon available for export (Cassar et al., 2015; Stanley et al., 2010). GPP is the amount of energy produced by primary producers (e.g., phytoplankton, ice algae) during a given time. NPP is the

difference between GPP and autotrophic respiration, while NCP is GPP minus respiration from both autotrophic and heterotrophic organisms.

The eastern Bering Sea shelf is a highly productive seasonal system with a dominant spring bloom that has long-lasting effects on the biological production of both pelagic and benthic consumers (Sigler et al., 2016; Springer et al., 1996). Primary production rates vary substantially across the shelf from the most productive areas along the shelf break (Codispoti et al., 2013; Lomas et al., 2020; Springer et al., 1996) to the lower productivity inner shelf regions (Cross et al., 2014; Mordy et al., 2012). Across the whole region, most carbon is produced during the spring bloom (Sigler et al., 2014) whose timing is well correlated with the timing of ice retreat, except in years when ice retreat occurs before mid-March (Brown & Arrigo, 2013; Sigler et al., 2014). Diatoms dominate spring blooms and provide an important, temporary, nutritional resource for both benthic and pelagic consumers, including benthic invertebrates (Copeman et al., 2021), and micro and meso-zooplankton grazers (Kimmel et al., 2018; Stoecker et al., 2014). During summer, the eastern Bering Sea shelf also experiences long periods of high stratification and depleted nitrogen concentrations in the surface waters (Hansell et al., 1993; Mordy et al., 2012) that suppresses phytoplankton growth and influences phytoplankton composition (Lomas et al., 2020; Moran et al., 2012; Sambrotto et al., 2008), with dinoflagellates and smaller phytoplankton becoming abundant in the surface waters (Moran et al., 2012). However, storms and wind mixing events interrupt these low production regimes by supplying nutrients from below the mixed layer to the surface ocean, supporting subsequent pulses of primary production (Eisner et al., 2016; Sambrotto et al., 1986; Stabeno et al., 2007). At the end of summer, a fall bloom commonly forms (Sigler et al., 2014) which enhances plankton production and provides critical dietary reserves for many organisms, such as copepods, prior to overwintering (Coyle & Gibson, 2017).

A long history of in situ sampling, has provided a fundamental understanding of the overall seasonal cycle (Lomas et al., 2020; Sambrotto et al., 1986; Sigler et al., 2014) and spatial variability of production rates (Codispoti et al., 2013; Springer et al., 1996) in the eastern Bering Sea ecosystem. Yet, fewer studies have estimated primary production dynamics at sub-seasonal resolution (days to weeks). By providing full seasonal estimates of GPP, NCP, and NPP rates, our study fills that gap, and aims to provide an improved understanding of how biogeochemical cycles, phytoplankton community growth rates, and community production of organic carbon vary during the growing season on the southeastern Bering Sea middle shelf. We quantify primary production over 4 yr (2016–2019) and NCP over 2 yr (2018–2019). Dissolved oxygen (O_2) is used to estimate GPP and NCP, and Chl-*a*, surface temperature and irradiance to model NPP. Data were collected from late April through early October using a Profiling Crawler (Prawler, Osse et al., 2015) that collects continuous vertical profiles of physical, dissolved oxygen, and Chl-*a* data from the surface to 50 m, typically in 2 hr intervals. In addition, data from moored sensors deployed at fixed depths during the cold season (October–April the following year) and in situ measurements collected from spring and fall research surveys were included. Our goals are to:

1. estimate GPP and NPP during 2016–2019, and NCP during 2018 and 2019 to assess phytoplankton production and carbon export fluxes at a high temporal resolution;
2. compare calculated phytoplankton community growth rates (p_{opt}^b) from the Prawler and more than 200 historical in situ values collected over 10 yr, and contrast these data with p_{opt}^b values derived from functional relationships based on temperature and Chl-*a* measurements (e.g., Behrenfeld & Falkowski, 1997; Kameda & Ishizaka, 2005);
3. assess to what extent summer phytoplankton community growth rates may be influenced by nitrate limitation.

2. Methods

We estimated GPP, NPP, and NCP in the southeastern Bering Sea, using sustained observations from the M2 mooring site (56.87°N, 164.07°W, Figure 1). This sampling site provides a good representation of biophysical conditions over the middle shelf (50–100 m depth) of the southeastern Bering Sea (Stabeno et al., 2001). Starting in 2016, a surface buoy was deployed adjacent to M2 in spring and summer (~late-April to early-October). A Prawler attached to the buoy mooring line collected vertical profiles of physical and biological data. The Prawler provided water column profiles of Chl-*a* ($\mu\text{g l}^{-1}$, Wetlabs EcoFluorometer FLNTU), O_2 ($\mu\text{mol } O_2 \text{ kg}^{-1}$, Aanderaa 4330 or 4330F), temperature ($^{\circ}\text{C}$), pressure and conductivity (SeaBird Electronic (SBE) Prawler-CTD), from the surface to ~50 m every 2 hr. Chl-*a* was calculated from fluorescence volts using factory calibrations. For these deployments, the Prawler was operated in two descending modes: a continuously descending profiling mode, and a “stop and hold” mode (only in 2018 and 2019). In the continuously descending mode, typically performed

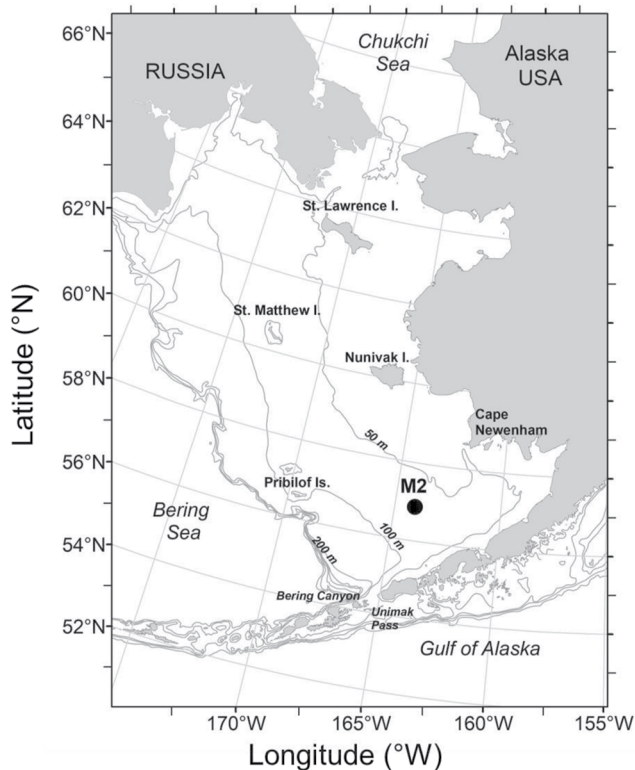


Figure 1. Map of the eastern Bering Sea showing the M2 mooring location (56.87°N, 164.05°W), and contours showing 50, 100, and 200 m (shelf break).

every 2 hr, the Prawler provides measurements at ~1 m vertical resolution as it descends from the surface to 50 m over a few minutes. In this mode, lags in both the salinity and O₂ optode sensors (Bittig et al., 2014) introduce errors at and below depths with thermal and oxygen stratification. Oxygen measurements below the mixed layer in these profiles were used for qualitative interpretation only. In the stop-and-hold mode, typically performed twice daily, the Prawler stops for several minutes during descent at a coarser series of fixed depths (~5 m resolution). The below mixed layer, salinity and O₂ data in this mode were considered reliable as the sensors had time to equilibrate at each depth. Data from a surface irradiance sensor (Eppley PSP, W m⁻²) was also available during summer deployments.

During the cold season (~early-October to late-April, data from fixed moorings) provided Chl-*a* (from fluorescence, Wetlabs EcoFluorometer FLNTU), O₂ (Aanderaa 3835 or 4831), temperature, pressure, and conductivity (SBE16, SBE37) measurements in the upper water column (~10–13 m). Discrete O₂ samples were collected at and around the M2 mooring during mooring deployment and recovery (April/May and September/October), and used to correct the moored O₂ sensor data (discussed below). Similarly, discrete surface (<10 m) Chl-*a* samples were collected and filtered through 25 mm Whatman GF/F filters (nominal pore size 0.7 μm). Filters were stored frozen (–80°C) and analyzed within 6 months with a bench top fluorometer following standard methods (Parsons, 1984). In association with the discrete samples, CTD casts also provided continuous vertical profiles of Photosynthetically Available Radiation (PAR, μmol photons m⁻² s⁻¹), temperature, pressure, and conductivity.

Lastly, we included data collected on the southern Bering Sea middle shelf, from more than 200 historical near-surface (<10 m) stable isotope (NaH¹³CO₃) deck incubations for in situ primary production and Chl-*a* discrete depth data

from 2006 to 2019 (data presented in Lomas et al., 2020). These measurements were used to calculate phytoplankton photosynthetic capacity (p_{opt}^b i.e., the normalized primary production to Chl-*a* ratio). The p_{opt}^b from these discrete samples was compared to Prawler-calculated p_{opt}^b (GPP/Chl-*a*) and model derived p_{opt}^b based on Chl-*a* and temperature (Kameda & Ishizaka, 2005) or temperature alone (Behrenfeld & Falkowski, 1997).

2.1. O₂ Data Processing

Pressure and salinity corrections were applied post-recovery to the oxygen concentration reported from each optode instrument. O₂ data were then processed to remove outliers, or due to sensor failure, or fouling, and corrected for slow multiyear decreases in instrument gain/sensitivity that occur with time and usage in this sensor type (Bittig et al., 2018). This correction was done by adjusting for the offset of the prawler O₂ concentration values, relative to in situ discrete water samples for O₂ (Figure S1 and Table S1 in Supporting Information S1), measured using Winkler titration techniques during the time of the deployments (1–2 days). All O₂ corrections resulted in increased sensor gain, consistent with the drift observed in other optode instruments (Bittig et al., 2018). In deployments where comparisons were available at mooring recovery, and residual drift was apparent, we assumed that the sensor gain declined linearly in time during deployment. While the decrease in optode sensitivity is not necessarily linear in time (Bittig et al., 2018, Figure 7), the time scales of drift are sufficiently long that assuming a linear decrease in sensitivity introduces only a very small amount of error. In addition, periods of the O₂ time-series showing abnormally high diel swings that could not be attributed to biological production or accounted for by physical processes were removed (see details in the Supporting Information S1).

Corrected O₂ data from each down cast Prawler profile that passed these quality checks and were not affected by optode sensor lags, were used to calculate the average O₂ of the surface mixed layer for that specific time point. On the southeastern Bering Sea middle shelf, the pycnocline and thermocline are coincident (Kara et al., 2000; Ladd & Stabeno, 2012), thus the mixed layer was defined as the depth at which there was a 0.2°C difference relative to the 5 m temperature measurement (Stabeno et al., 2010). The 5 m reference depth was chosen to reflect

a shallowest consistent depth at which Prawler profile data were available. Average surface to mixed layer O₂ concentrations from each two hourly profile were then linearly interpolated to hourly intervals to produce full daily O₂ concentration cycles necessary for the GPP Fourier calculations. Similarly, quality assessment, average calculations, and hourly interpolation were done for Chl-*a*, temperature, and salinity. The fixed mooring O₂ data were quality corrected in a similar way, except no water column averaging over the mixed layer was done, and 15 min measurements were averaged to form hourly estimates.

2.2. Primary Production Calculations

Our analysis consisted of estimates of GPP, NPP, and NCP. Note that in most cases the estimates were smoothed using 5-day averaging, or calculated as weekly or monthly estimates. Such averaging was considered appropriate when comparing different production terms that may integrate over slightly different time-scales. For comparison between O₂ derived (GPP, NCP) and carbon derived (NPP) production estimates we used a photosynthetic quotient (PQ) conversion factor of O₂:C of 1.4:1 (Freitas et al., 2020; Hedges et al., 2002). Throughout, p_{opt}^b values were calculated as the quotient of normalized production to Chl-*a*, in units mg C mg Chl-*a*⁻¹ hr⁻¹. PAR was estimated in μmol photons m⁻² s⁻¹ by converting from measured short-wave downwelling radiation (Watts m⁻²), using a conversion factor of 4.57, and assuming that 43% of shortwave radiation was available for photosynthetic organisms (Jerlov, 1976). Daily production estimates were calculated as a volumetric average (NCP and GPP: mmol O₂ m⁻³ day⁻¹ and NPP: mg C m⁻³ day⁻¹) from the surface to the depth of the mixed layer, while integrated production values (m⁻² day⁻¹) were calculated, by integrating the volumetric averages from the surface to the mixed layer depth.

Estimates of GPP were done using high-frequency Fourier analysis of O₂ (Cox et al., 2015). This method follows,

$$GPP(t) \approx 2\omega_1 \frac{\sin \theta - \theta \cos \theta}{\theta - \frac{1}{2} \sin 2\theta} A_{O_2}, \quad (1)$$

where $\theta = \pi f_{\text{DL}}$, with f_{DL} being the fraction of hours during the day where light is present, and ω_1 the diurnal frequency (hours) and A_{O_2} the Fourier amplitude (ΔO_2) at the diurnal frequency (Cox et al., 2015). The Fourier amplitude thus represents the intensity of the recurring O₂ signal at 24 hr (i.e., diurnal frequency, Cox et al., 2015). Community respiration is here assumed to be constant and thus does not contribute to the diel amplitude in the 24 hr frequency domain. For a full explanation of the method see Cox et al. (2015). Implementation was done using the R-package “GPPfourier” (Cox, 2017) on the hourly O₂ data, and using a complex demodulation smoothing technique which lowers the influence of short-term physical processes on the O₂ concentration time series (Cox et al., 2017). Uncertainties of the GPP Fourier estimates were calculated using a Monte Carlo simulation approach that included independent random noise terms for O₂ vertical gradients and within-day variation of community respiration, sensor correction, air-sea flux, and turbulence (Figure S2 in Supporting Information S1); see Supporting Information S1 for full details.

2.3. NPP Estimation

NPP calculations were done using the daily mooring data applied to the productivity model from Behrenfeld and Falkowski (1997), following:

$$NPP = \text{Chl} \times p_{\text{opt}}^b \times \text{DL} \times \left[\frac{0.66125 \times E_0}{E_0 + 4.1} \right] \quad (2)$$

where, Chl is the surface ocean Chl-*a*, p_{opt}^b the biomass-specific photosynthesis capacity, DL is the day length in hours and E_0 is averaged daily surface PAR. Estimates were calculated as the volumetric average within the mixed layer. The E_0 was based on the average daily PAR calculated from measurements at the top of the mooring buoy approximately 3 m above the sea surface. We derived daily p_{opt}^b estimates using the approach recommended by Kameda and Ishizaka (2005) that relates both temperature and Chl-*a* biomass levels to photosynthetic capacity. This approach, is based on the premise that periods with large Chl-*a* biomass are also commonly dominated by large cells that tend to have higher photosynthetic capacity (Uitz et al., 2008), something that is the case on the eastern Bering Sea shelf, particularly during bloom periods (Eisner et al., 2016; Lomas et al., 2020). Uncertainties of the NPP estimates were calculated using a Monte Carlo simulation approach (Supporting Information S1).

2.4. NCP Estimation

NCP was estimated by comparing the change of surface O_2 concentration at longer than diel time scales to the cumulative addition or removal of oxygen due to physical processes; the difference between these is equated to net biological (community) production (Emerson & Stump, 2010). The mixed layer balance considered here included physical inputs due to surface gas exchange with the atmosphere (GE), turbulent exchange between the mixed layer and interior (TE), and vertical fluid motion relative to the mixed layer base (FMLB; i.e., entrainment or de-entrainment):

$$NCP_{ML} = \frac{\partial [O_2]_a}{\partial t} - GE - TE - FMLB, \quad (3)$$

where $[O_2]_a$ is the average O_2 concentration within the mixed layer. The parameterization of each term and the methods used in their estimation are described in detail in Supporting Information S1. Time-varying values for each physical term on the right-hand side of Equation 3 were used to estimate the residual NCP_{ML} , which was subsequently low-pass filtered with a 60 hr half-cosine filter and subsampled at daily intervals. Horizontal advection was not considered due to lack of information on horizontal O_2 gradients, and because mean flows on the southeastern Bering Sea shelf near M2 are generally weak in the summer months (Stabeno et al., 2010). This term is therefore likely to be small relative to the magnitude of NCP. Surface GE was estimated using the parameterization of Liang et al. (2013), where the partially and fully collapsing bubble flux terms in this parameterization were reduced by multiplying by a constant factor of 0.37, following Emerson et al. (2019). Turbulent exchange was parameterized using time-varying diffusivity (K_z) values that were estimated as a residual in the corresponding mixed layer temperature balance (Cronin et al., 2015) using the Prawler data. The resulting diffusivities are of order 10^{-5} – 10^{-4} $m^2 s^{-1}$, which is typical of values within the stratified lower oceanic boundary layer (Sun et al., 2013, see also the Supporting Information S1). Upwelling at the mixed layer base was assumed to be driven by Ekman pumping or suction, which was determined using wind stress curl from the ERA5 atmospheric reanalysis (Hersbach et al., 2018). Vertical gradients in O_2 for NCP calculations were estimated using stop-and-hold profiles. The availability of the stop-and-hold data also facilitated water column integrated NCP estimates from the surface to 72 m (the water depth at the deployment site in 2018 and 2019):

$$NCP_{72} = \frac{\partial [O_2]_{int}}{\partial t} - GE - UPW - FSED, \quad (4)$$

where here, $[O_2]_{int}$ is the vertically integrated, full-depth oxygen content, UPW represents upwelling due to local wind stress curl, and FSED represents the flux of oxygen at the ocean bottom which is assumed to be downward and sufficient to balance the consumption of oxygen within the sediments (Cross et al., 2014; Rowe & Phoel, 1992). Specifically, rates of respiration reported for the middle shelf in 2008–2010 by Cross et al. (2014) were used as the bottom boundary condition in the 72 m oxygen balance. Mixed layer NCP was estimated from 15 May to 29 September 2018 and from 2 May to 7 July 2019. Full-depth NCP in 2018 was estimated from 2 May to 27 August (final stop-and-hold profile) in 2018 and from 2 May to 7 July 2019. Uncertainties of the NCP calculations were estimated using a Monte Carlo procedure (500 iterations, Pelland et al., 2018), which considered errors due to O_2 sensor accuracy, gas exchange, vertical gradients, diffusivity, sediment respiration, estimation of local rates of change, and unresolved advection (in Supporting Information S1).

2.5. Nitrogen Stress Calculations

To assess if phytoplankton production appeared to be nitrogen limited during the growing season we calculated a probability index of apparent nitrogen stress, by calculating the difference between phytoplankton nitrogen demand and nitrogen availability. Nitrogen demand was calculated based on both Prawler GPP estimates and previous in situ measured carbon-based production rates ($mg C m^{-3} day^{-1}$), and converted to N production rates. The GPP estimates from the Prawler, were converted to carbon-based production assuming a PQ of 1.4:1 ratio, and assuming an NPP:GPP ratio of 0.7 (Carvalho et al., 2017; Spilling et al., 2019). The production data, both the in situ measured and prawler based rates, were then converted to nitrogen production ($mg N m^{-3} day^{-1}$) assuming a particulate organic nitrogen (PON) to particulate organic carbon (POC) ratio of 0.115. PON:POC ratio data were calculated based on the sum of ammonium (NH_4^+) and nitrate (NO_3^-) uptake rates using stable isotope primary production data from past research cruises (data presented in Lomas et al., 2020).

Nitrogen availability, determined using concentrations (mg N m^{-3}), was obtained from long-term monitoring efforts. This includes 3,672 previously collected samples in the upper (≤ 10 m) water column on the southern (55° – 60°N) shelf between 2003 and 2018. The different expeditions, protocols, and techniques used to collect and process samples for dissolved inorganic nitrogen (NO_3^- and NH_4^+) are described in Mordy et al. (2021). Historically, sampling of discrete primary production and nutrients data has been concentrated around spring (April–May) and late summer/early fall (August–September), thus our analyses included more values from those months. For all empirically measured nitrogen concentrations, primary production and PON:POC ratios, we used data from the southeastern Bering Sea middle shelf ($<60^{\circ}\text{N}$, 50–100 m isobaths) from surface to 10 m.

Data on both nitrogen inventories and production were strongly non-normal in their distribution. We therefore used a bootstrap approach that simulated the probability that any nitrogen production value was above or below a given nitrogen concentration measurement. Resampling with replacement was done for each month and run for 1,000 simulations. The output of these analyses was considered a probability of phytoplankton experiencing nitrogen stress, with values of 0 indicating no stress and a value of 1 suggesting full nitrogen stress. Because archived in situ data covered over a decade of observations, the analysis of nitrogen stress provided an average categorization of the seasonal cycle across multiple years. All data analyses were performed with the statistical software R 3.6 (R Core Team, 2018) or MATLAB version R2020a (The Mathworks, Inc.).

3. Results

Prawler profiles from surface to 50 m clearly illustrated the seasonal bloom progression. The formation of a clear two-layer system with typical surface mixed layer depths of 8–25 m was common for all years in early summer (Figure 2). Surface temperatures in all 4 yr reached 12°C – 14°C during summer and bottom temperatures in summer were typically 2°C – 5°C , except in 2017, the year with the greatest southward sea-ice extent, where temperatures were closer to 0°C . O_2 saturation values, were highest ($>120\%$) in the upper mixed layer and during the peak of the spring phytoplankton bloom. In 2017, Prawler measurements commenced after the spring bloom but noticeably high O_2 saturation remained in surface waters to a depth of ~ 30 m. After the bloom, O_2 saturation values were close to 100% in the upper ocean, while O_2 saturation values below the mixed layer depth were commonly 75%–95%. During the spring bloom, Chl-*a* reached high values ($>10 \mu\text{g l}^{-1}$) in the upper ocean (Figure 2); these elevated values were visible from the surface to the mixed layer depth. After the main spring bloom peak, Chl-*a* levels were generally low ($<2\text{--}3 \mu\text{g l}^{-1}$), and commonly with the highest values near the thermocline suggesting that small subsurface Chl-*a* maxima were common throughout summer. Following the bloom, some brief periods of more modest Chl-*a* accumulation and elevated O_2 saturation were also apparent in some years (e.g., early September 2017, late August 2018; Figure 2). While the bloom in 2017 occurred prior to the Prawler deployment, the main bloom was visible in a fluorometer (~ 11 m deep) on the fixed winter mooring (Figure 3). In 2017, the only year where sea ice reached as far south as M2, elevated Chl-*a* values were present at depths from ~ 25 to 40 m (also seen in a fixed fluorometer at 40 m deep) for over 4–7 weeks following the spring bloom maximum (Figure 2).

3.1. Seasonal Cycles and Weekly Averaged Production Estimates

Chl-*a* concentrations and O_2 derived GPP measurements in the upper mixed layer during summer and those derived from fixed moored sensors during winter (Figure 3) showed spring bloom peak timing around 9 May (2016), 25 April (2017), 1 June (2018), and 8 May (2019). These analyses also showed that the bloom in 2016 and 2017 occurred just prior to the Prawler deployment, as high Chl-*a* and O_2 values were captured by the overwintering fixed depth mooring instrumentation. GPP during the spring bloom varied from ~ 35 to $70 \text{ mmol O}_2 \text{ m}^{-3} \text{ day}^{-1}$ across all 4 yr, while smaller short-term peaks usually reached around $15\text{--}20 \text{ mmol O}_2 \text{ m}^{-3} \text{ day}^{-1}$ at times throughout the summer. Background levels during non-bloom conditions were $\sim 5\text{--}10 \text{ mmol O}_2 \text{ m}^{-3} \text{ day}^{-1}$.

3.2. Water Column Integrated NCP Rates

Surface mixed layer (surface to the mixed layer depth) and full water column (surface to 72 m) integrated NCP rates were calculated for 2018 (May–September) and 2019 (May–July, Figure 4). In the mixed layer balance, GE is the dominant resolved physical term in both years (Figures S3a–S3b in Supporting Information S1). Local

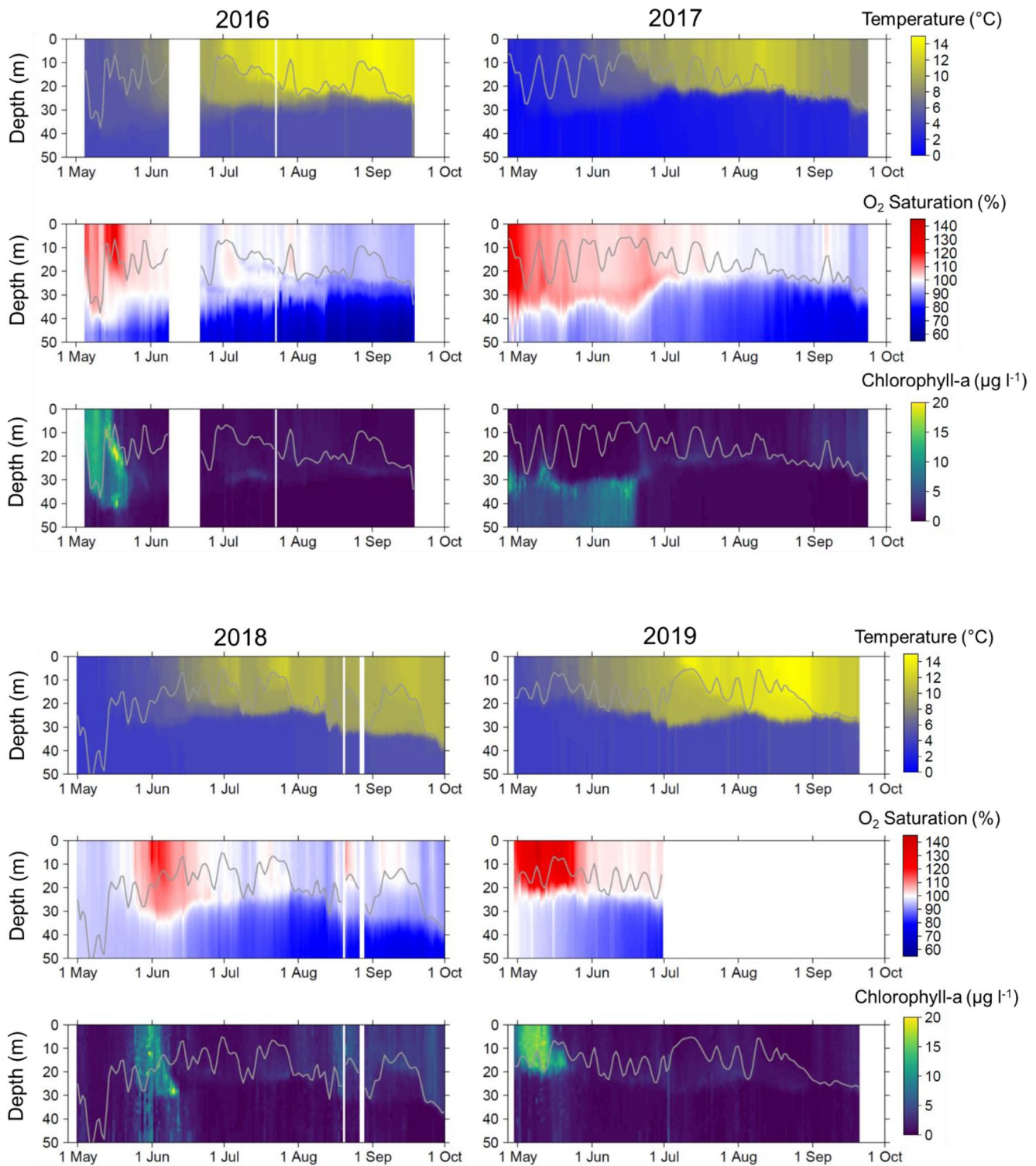


Figure 2. Prawler profiles of temperature, O_2 saturation, and chlorophyll- a for 2016–2019. In all plots, the gray line denotes the mixed layer depth estimated as $\delta T = 0.2^\circ\text{C}$ difference from 5 m temperature.

accumulation of oxygen in the ML does occur during the bloom period, but declines seasonally thereafter as the surface ocean warms. The TE and FMLB terms are secondary in the ML overall, but can be important for brief periods of abrupt changes in MLD (e.g., near 1 June 2018, Figure S3a in Supporting Information S1). In the full-depth balance, GE and loss of oxygen from the water column are both leading terms, with the assumed loss

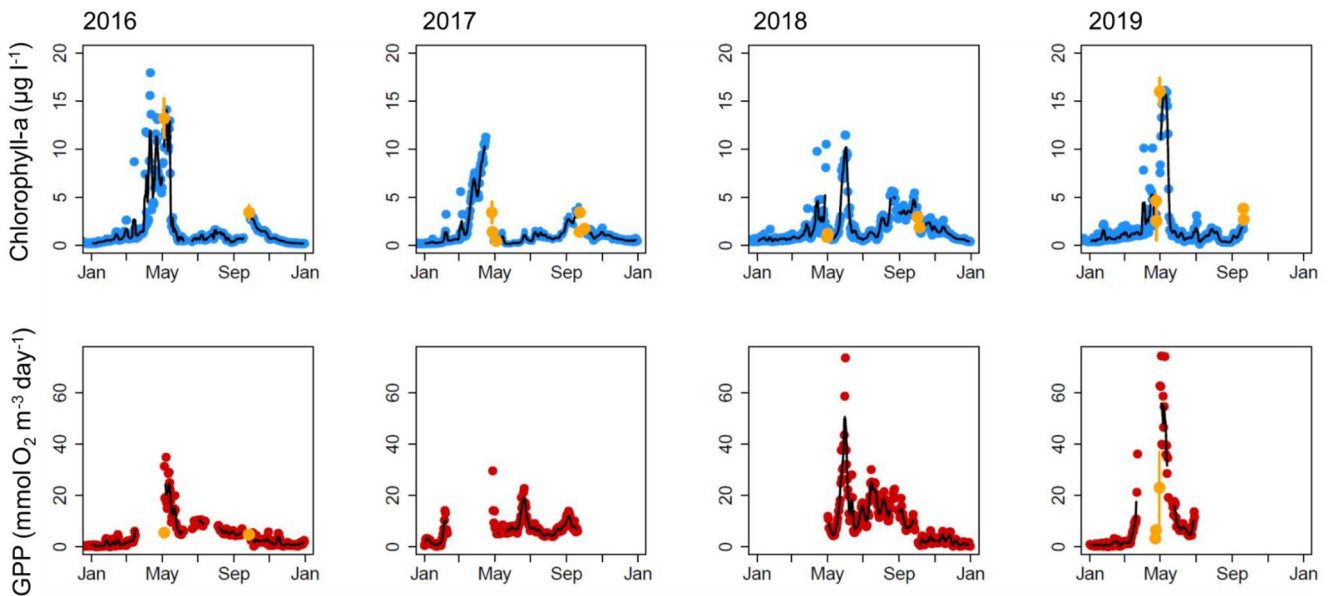


Figure 3. Seasonal profiles of chlorophyll-*a* ($\mu\text{g l}^{-1}$, blue), and gross primary production (GPP, $\text{mmol O}_2 \text{ m}^{-3} \text{ day}^{-1}$, red) based on the average of data from surface to the mixed layer depth for summer (May–September). Measurements from winter deployments, (January–April and October–December) used data from a fixed sensor (depth range among years: 9–13 m). Points denote daily estimates, black lines denote 5-day smoothed averages. Yellow circles denote average ($\pm\text{SD}$) (top panel) discrete sample chlorophyll-*a* ($\mu\text{g l}^{-1}$) or (bottom panel) primary production ^{13}C bottle measurements converted to $\text{mmol O}_2 \text{ m}^{-3} \text{ day}^{-1}$, from $\text{mg C m}^{-3} \text{ day}^{-1}$, using $\text{O}_2\text{:C}$ of 1.4:1.

to sediments, FSED, a secondary but persistent term that provides an offset by the end of summer 2018 (Figures S3c–S3d in Supporting Information S1). Highest NCP rates occurred during the spring bloom, reaching above 400 (2018) and 600 (2019) $\text{mmol O}_2 \text{ m}^{-2} \text{ day}^{-1}$. The similar magnitudes of the surface and full water column NCP rates during the bloom indicated that most community production of organic carbon occurred in the surface ocean. After the spring bloom, NCP rates were generally low ($<100 \text{ mmol O}_2 \text{ m}^{-2} \text{ day}^{-1}$) and at times negative in the surface layer. When differences between the mixed layer and full water column rates of NCP were apparent, for example, June 2018, the full water column rate was almost always lower or more negative than the mixed layer rate, indicative of net respiration of O_2 between the mixed layer and the bottom (Figure 4). Following the spring bloom, full water column NCP values were most commonly negative indicating net heterotrophic conditions (Figure 4).

3.3. GPP, NPP, and NCP Carbon Budgets

Weekly averages of GPP, NPP (2016–2019), and NCP (2018 and 2019) upper water column production rates aligned with overall expectations (Y. Huang et al., 2021; Spilling et al., 2019), as GPP was greater than NPP, which in turn was greater than or equal to NCP (Figure 5). In the years 2018 and 2019, when the Prawler fully captured the spring bloom period, GPP rates reached 350–450 $\text{mg C m}^{-3} \text{ day}^{-1}$ (Figures 5c and 5d, Table 1). In 2016, the Prawler captured the latter part of the bloom with values close to 200 $\text{mg C m}^{-3} \text{ day}^{-1}$ (Figure 5a), while in 2017, the Prawler was deployed after the spring bloom (Figure 5b). NPP rates reached 150 $\text{mg C m}^{-3} \text{ day}^{-1}$ in 2016, 200 $\text{mg C m}^{-3} \text{ day}^{-1}$ in 2018, and $\sim 280 \text{ mg C m}^{-3} \text{ day}^{-1}$ in 2019. During the bloom period, NCP rates reached $\sim 190 \text{ mg C m}^{-3} \text{ day}^{-1}$ in 2018 and $\sim 280 \text{ mg C m}^{-3} \text{ day}^{-1}$ in 2019 (Figures 5c and 5d). After the bloom, GPP generally varied from 100 to 200 $\text{mg C m}^{-3} \text{ day}^{-1}$, while NPP remained below 70 $\text{mg C m}^{-3} \text{ day}^{-1}$ except in August–October of 2018. Common for 2017 were low NPP above the mixed layer (Figure 5b), mainly due to low Chl-*a* levels in the surface ocean (Figures 2 and 3).

NPP:GPP (average \pm SD) during the 2 weeks centered around the spring bloom were 0.83 ± 0.26 , 0.49 ± 0.12 , and 0.63 ± 0.23 for 2016, 2018, and 2019, respectively (Table 1). NCP:GPP ratios during the 2 weeks centered around the spring bloom were 0.38 ± 0.17 and 0.50 ± 0.16 in 2018 and 2019, respectively. During non-bloom conditions, monthly NPP:GPP commonly ranged from 0.30 to 0.60 during the 4 yr (Table 1). Exceptions were low NPP:GPP ratios (<0.2) occurring in May and June 2017, when almost all Chl-*a* was present below the mixed

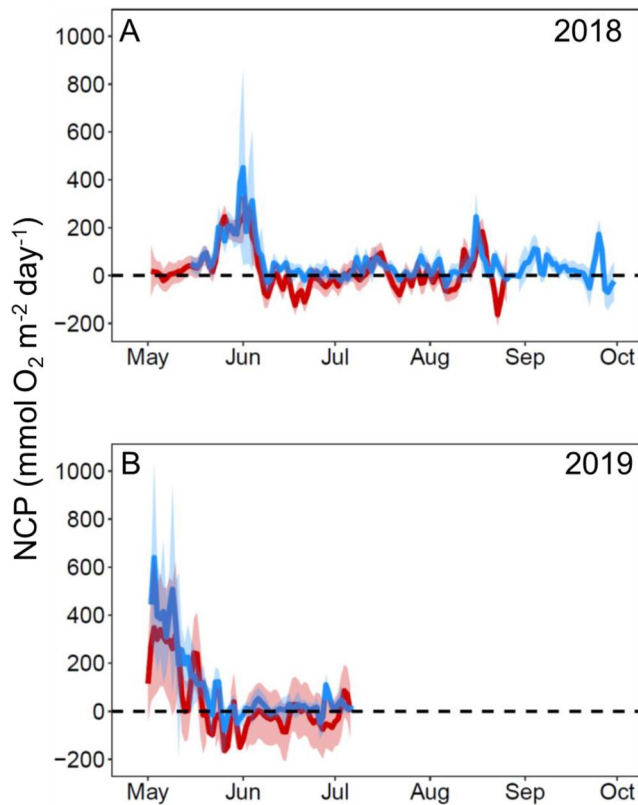


Figure 4. Vertically integrated net community production (NCP, $\text{mmol O}_2 \text{ m}^{-2} \text{ day}^{-1}$) in the upper ocean (surface to mixed layer, blue) and from surface to 72 m (red), for (a) 2018 and (b) 2019. Dashed line is used to designate positive (net autotrophic) and negative (net heterotrophic) NCP. Shaded areas show bootstrap estimated uncertainties.

layer, and in September 2018 when the NPP:GPP ratio was greater than 0.7. Monthly NCP:GPP ratios in non-bloom conditions were generally below 0.16 for 2018–2019 (Table 1).

During the 2 weeks centered around the bloom, autotrophic respiration (GPP minus NPP) rates were 32–181 $\text{mg C m}^{-3} \text{ day}^{-1}$ for 2016–2019, while community respiration rates were 201 and 206 $\text{mg C m}^{-3} \text{ day}^{-1}$ in 2018 and 2019, respectively. In all the years, monthly averaged autotrophic respiration rates during non-bloom conditions commonly ranged from 25 to 80 $\text{mg C m}^{-3} \text{ day}^{-1}$. Monthly averaged community respiration during non-bloom conditions ranged from 53 to 127 $\text{mg C m}^{-3} \text{ day}^{-1}$ in 2018 and 2019, respectively. A comparisons using data from 2018, showed that estimates of community respiration (GPP minus NCP) aligned well with estimates based on daily night time O_2 rate of change (Figure S5 in Supporting Information S1). Weekly averaged Chl-*a* and NCP:GPP ratios, and Chl-*a* and NCP were positively correlated (Figure 6), indicating a greater efficiency of net carbon fixation relative to primary production in the upper ocean with increasing Chl-*a*. These relationships also indicated that, eventually, NCP reaches a threshold of ~50%–60% of GPP, and furthermore that there is a minimum GPP threshold before any noteworthy NCP occurs.

3.4. Photosynthetic Capacity (p_{opt}^b) and Nutrient Stress Calculations

Prawler photosynthetic capacity ($p_{\text{opt_prawler}}^b$) was calculated using the Prawler GPP estimate derived from the O_2 data and Chl-*a* concentrations. The average derived $p_{\text{opt_prawler}}^b$ generally increased from spring (~2.5–3.0) to summer (except in 2017), remaining relatively high (3.5–6.0) into June and July because of relatively low Chl-*a* values (Figures 3 and 7a–7d, red bars). Later in summer, lower $p_{\text{opt_prawler}}^b$ values (<2.5) were commonly observed but at variable time periods during July–September. $p_{\text{opt_prawler}}^b$ values were lowest during August–September in 2016, 2017, and 2018. Exceptions to these general patterns were high (>9) May and June $p_{\text{opt_prawler}}^b$ values in 2017, driven

by the high GPP and low Chl-*a* surface values. Comparisons to p_{opt}^b values derived from temperature or from Chl-*a* and temperature showed the largest discrepancy in late summer, indicating that factors other than temperature and phytoplankton biomass regulated growth (Figures 7a–7d). The same pattern of depressed phytoplankton growth in late summer to early fall was also visible in the compiled historical p_{opt}^b data based on discrete sample measurements between 2006 and 2019 (Figure 7e). The p_{opt}^b values derived from models using temperature or Chl-*a* and temperature relationships aligned fairly well with discrete sample estimates in spring and mid-summer, but were substantially higher (>4.0) in late summer compared to the historical (<2.5) p_{opt}^b discrete sample values (Figure 7c).

To assess if phytoplankton growth was nitrogen limited we calculated apparent nitrogen stress as a probability index of nitrogen demand exceeding nitrogen availability (Figure 7f). For the Prawler based estimates, nitrogen stress was low in spring before increasing in June and remaining above 0.5 until September (Figure 7f). Nitrogen stress values from the discrete sample data were low from April to July, before increasing in August and September. However, the number of estimates from June ($N = 6$) and July ($N = 10$) were low and based on data from a few cruises in 2008–2010. Overall, the nitrogen stress estimates suggest that the primary period of apparent nitrogen limitation for phytoplankton growth appears to occur during mid to late summer.

4. Discussion

Continuous temporal physical and biological measurements from moored instruments, as utilized here, allowed the quantification of seasonal variations in GPP, NPP, and NCP rates. In most cases, the three productivity metrics aligned well with general expectations in terms of production magnitudes (Codispoti et al., 2013; Giesbrecht et al., 2019; Springer et al., 1996) and the balances between each term (Y. Huang et al., 2021; Regaudie-de-Gioux

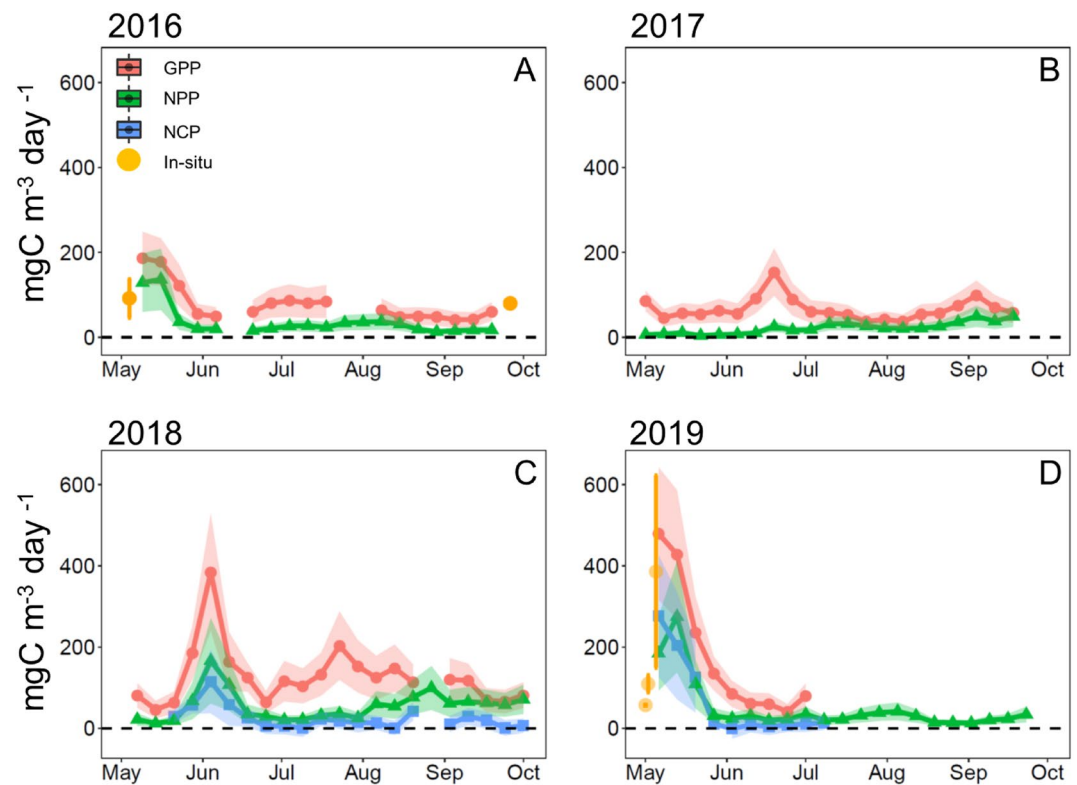


Figure 5. Comparison of weekly upper ocean averages of the 5-day smoothed estimates of gross primary production (GPP, red), net primary production (NPP, green), and net community production (NCP, blue, only 2018–2019) in units of $\text{mg C m}^{-3} \text{ day}^{-1}$ for (a) 2016, (b) 2017, (c) 2018, and (d) 2019. Discrete sample primary production measurements taken near the mooring site are shown by yellow dots (mean \pm 1 SD). Shaded areas for GPP, NPP, and NCP show bootstrap estimated uncertainties. Dissolved oxygen units were converted to carbon using a 1.4:1 conversion coefficient.

& Duarte, 2013). Overall, our analyses showed clear agreements in the estimates of peak bloom timing based on GPP, NPP, NCP rates, and standing stock of Chl-*a*. High NCP values, and high NCP:GPP ratios (>0.4), are consistent with the majority of the production of organic carbon occurring in association with the spring bloom period, as also observed previously (Prokopenko et al., 2011; Sambrotto et al., 1986). The variable but general reduction of primary production rates in late summer and early fall appeared to be due to nitrogen limitation.

4.1. Uncertainties of Production Estimations

Analyses of continuous O_2 and Chl-*a* data to derive measures of production, as done here, are promising ways to enhance understanding of seasonal phytoplankton dynamics. Nonetheless, there are uncertainties with our analyses. Though the majority of production occurs in the upper part of the water column (Lomas et al., 2012), our analyses, except for NCP, did not capture processes below the mixed layer due to difficulty in accounting for optode sensor lag times during each Prawler downcast. Analyses of GPP using diel O_2 fluxes assume that this signal is primarily due to biological processes, however, physical processes have small but variable influences on the O_2 fluxes throughout the year (Staehr et al., 2012). The GPP Fourier method assumes that there are no systematic diurnal variations in respiration rates, O_2 fluxes through boundary layers, and that there are no O_2 gradients in the upper mixed layer (Cox et al., 2015). The error from the vertical O_2 gradients in the upper mixed layer was low ($\sim 5\%$ of total error) except for during the bloom. Overall, the influence of these combined sources of error was about 15%–20% of the total GPP estimates. However, community respiration, which was the largest source of uncertainty ($\sim 50\%$ of all errors), can be higher during the daytime hours (Mesa et al., 2017; Regaudie-de-Gioux & Duarte, 2012) introducing additional uncertainty particularly during the bloom period. If respiration was consistently higher during the day time this may have led to underestimations in GPP estimates. Another source of uncertainty arises from the fact that PQ values ($\text{O}_2:\text{C}$ ratios) vary depending on the nitrogen substrate fueling production (Laws, 1991). For the open ocean, these values range from 1.1 to 1.4 (Laws, 1991),

Table 1

Overview of Bloom and Monthly Average Surface to Mixed-Layer, Production Rates, Ratios and Respiration Rates ($\text{mg C m}^{-3} \text{ day}^{-1}$, Mean \pm Standard Deviation [SD])

| Year | Seasons | GPP \pm SD | <i>N</i> | NPP \pm SD | <i>N</i> | NCP \pm SD | <i>N</i> | NPP:GPP \pm SD | <i>N</i> | NCP:GPP \pm SD | <i>N</i> | Condition |
|------|----------------|-------------------|-------------------|------------------|----------|-------------------|----------|------------------|----------|------------------|----------|-------------------------|
| 2016 | Bloom (9 May) | 197.0 \pm 57.8 | 12 | 167.3 \pm 69.5 | 6 | | | 0.83 \pm 0.26 | 6 | | | |
| 2018 | Bloom (1 June) | 308.6 \pm 126.6 | 14 | 145.4 \pm 48.0 | 14 | 107.5 \pm 59.4 | 14 | 0.49 \pm 0.12 | 14 | 0.36 \pm 0.17 | 14 | |
| 2019 | Bloom (8 May) | 423.8 \pm 128.6 | 14 | 242.5 \pm 45.7 | 14 | 217.8 \pm 112.4 | 14 | 0.63 \pm 0.23 | 14 | 0.49 \pm 0.16 | 14 | |
| 2016 | May | 138.7 \pm 70.4 | 27 | 71.8 \pm 74.1 | 20 | | | 0.50 \pm 0.27 | 20 | | | End of bloom |
| 2016 | June | 60.8 \pm 17.4 | 12 | 20.8 \pm 4.0 | 18 | | | 0.38 \pm 0.11 | 12 | | | Post bloom |
| 2016 | July | 83.5 \pm 6.5 | 14 | 29.0 \pm 5.8 | 29 | | | 0.32 \pm 0.06 | 14 | | | Post bloom |
| 2016 | August | 52.3 \pm 8.3 | 27 | 26.6 \pm 10.7 | 31 | | | 0.47 \pm 0.17 | 27 | | | Post bloom |
| 2016 | September | 43.1 \pm 6.3 | 15 | 16.6 \pm 2.3 | 17 | | | 0.39 \pm 0.08 | 15 | | | Post bloom |
| 2017 | May | 67.6 \pm 41.4 | 28 | 7.6 \pm 3.5 | 31 | | | 0.14 \pm 0.08 | 28 | | | Post bloom ^a |
| 2017 | June | 95.4 \pm 42.1 | 30 | 14.9 \pm 7.8 | 30 | | | 0.16 \pm 0.04 | 30 | | | Post bloom ^a |
| 2017 | July | 51.5 \pm 10.7 | 31 | 26.9 \pm 7.5 | 31 | | | 0.55 \pm 0.20 | 31 | | | Post bloom |
| 2017 | August | 52.7 \pm 13.4 | 31 | 24.9 \pm 6.3 | 31 | | | 0.48 \pm 0.09 | 31 | | | Post bloom |
| 2017 | September | 78.6 \pm 20.7 | 20 | 43.9 \pm 13.3 | 23 | | | 0.60 \pm 0.17 | 20 | | | Post bloom |
| 2018 | May | 137.8 \pm 120.9 | 30 | 51.1 \pm 56.4 | 31 | 64.5 \pm 61.5 | 18 | 0.33 \pm 0.10 | 28 | 0.34 \pm 0.16 | 18 | Pre bloom |
| 2018 | June | 141.6 \pm 115.8 | 30 | 57.8 \pm 56.8 | 30 | 29.9 \pm 46.4 | 30 | 0.39 \pm 0.19 | 30 | 0.15 \pm 0.19 | 30 | Bloom |
| 2018 | July | 144.7 \pm 49.4 | 31 | 31.2 \pm 9.3 | 31 | 14.0 \pm 19.8 | 31 | 0.23 \pm 0.09 | 31 | 0.11 \pm 0.15 | 31 | Post bloom |
| 2018 | August | 139.4 \pm 31.0 | 24 | 73.6 \pm 24.4 | 28 | 18.1 \pm 28.5 | 26 | 0.47 \pm 0.15 | 16 | 0.14 \pm 0.22 | 24 | Post bloom |
| 2018 | September | 85.1 \pm 26.7 | 28 | 63.2 \pm 13.2 | 31 | 14.6 \pm 19.3 | 29 | 0.80 \pm 0.20 | 26 | 0.16 \pm 0.22 | 28 | Post bloom |
| 2019 | May | 288.9 \pm 183.4 | 130.1 \pm 106.7 | 31 | 32 | 120.7 \pm 125.9 | 25 | 0.49 \pm 0.25 | 25 | 0.32 \pm 0.35 | 25 | Bloom |
| 2019 | June | 60.7 \pm 18.9 | 29 | 27.1 \pm 8.4 | 30 | 8.0 \pm 10.9 | 30 | 0.46 \pm 0.13 | 29 | 0.14 \pm 0.16 | 29 | Post bloom |
| 2019 | July | | | 34.6 \pm 18.6 | 31 | | | | | | | |
| 2019 | August | | | 20.7 \pm 11.1 | 31 | | | | | | | |
| 2019 | September | | | 24.3 \pm 7.3 | 19 | | | | | | | |

Note. *N* denotes the number of daily measurements in each month. Bloom data in 2016, 2018, and 2019 denote the 14 average rates and ratios centered around the spring bloom peak timing (date noted in table). In 2016, the Prawler just covered the latter part of the bloom reducing *N* for gross primary production (GPP) and net primary production (NPP). There are no bloom estimates from 2017 as the spring bloom occurred prior to the Prawler deployment. Conditions denote the month relative to the time of the spring bloom. NCP is calculated only for 2018 and 2019.

^aDenote a post-bloom with a subsurface chlorophyll-*a* maximum.

while values in more productive arctic and sub-arctic systems appear to be closer to 1.4 (Freitas et al., 2020; Platt et al., 1987). Here, we used a constant PQ value for GPP conversion of 1.4. While we did not have data to feasibly use a time-varying PQ value, it is indeed likely that, PQ values vary seasonally. In the Bering Sea PQ values are likely closer to 1.4 in spring (nitrate fueled) and closer to 1.1 in summer (ammonium fueled, Cheng et al., 2016; Mordy et al., 2012). A test, using the 2018 analyses showed that changing the GPP PQ value, from 1.4 to 1.2, resulted in higher total carbon derived GPP by \sim 16%. Similarly, it decreased NPP: GPP and NCP:GPP ratios by 16%. Despite these uncertainties, our GPP and NPP values derived from O₂ and Chl-*a* measurements appeared to align well, and similarly, ratios among GPP, NPP, and NCP were within expected ranges (Y. Huang et al., 2021; Prokopenko et al., 2011; Stanley et al., 2010), except for a few cases in late summer.

For the NCP calculations, we assumed constant benthic carbon consumption rates, an assumption that is supported by previous Bering Sea estimates (Cross et al., 2014). We tested this assumption by allowing all oxygen demand to have occurred from 2 May to 7 June but leaving the integrated FSED value unchanged. That leaves the full-depth summer-integrated NCP unchanged, but increases the net NCP prior to 7 June by 0.9 mol O₂ m⁻² (an increase of \sim 30%). The net NCP then decreased by the same value following this date, adding to the weak net water column oxygen consumption observed overall in 2018 post-bloom. These modifications, which assume an extreme partitioning of sedimentary respiration seasonally, did not qualitatively alter the comparison between

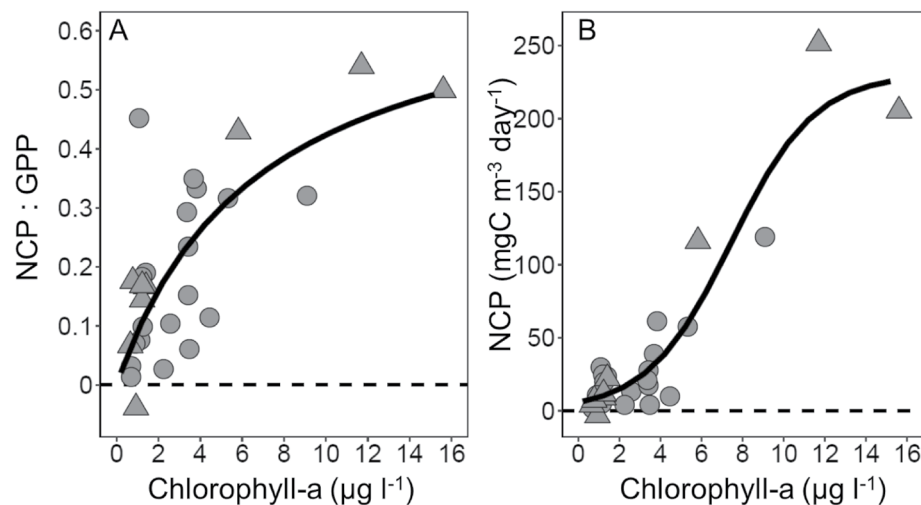


Figure 6. Weekly averages of (a) Chlorophyll-*a* plotted against the ratio of NCP:GPP ($p < 0.01$, degrees freedom (df) = 26), and (b) net community production (NCP) ($p < 0.01$, df = 25) for 2018 (circles) and 2019 (triangles). Trend lines plotted as (a) a saturating function and (b) sigmoid relationship based on functional relationships shown in previous analysis (K. Huang et al., 2012). Dissolved oxygen units converted to carbon using a 1.4:1 conversion coefficient.

full-depth and mixed layer NCP which assumed a constant benthic carbon consumption rates. Overall, by incorporating realistic uncertainty estimates and excluding data when clear physical influences (e.g., advection) were present, our analyses using O_2 and Chl-*a* data show that profiling moorings are well suited for retrieving concurrent estimates of GPP, NPP, and NCP at daily to weekly seasonal resolutions.

4.2. GPP, NPP, and NCP Rates During Spring and Summer

The spring bloom period is crucial for fueling higher trophic-level production (Hunt et al., 2011; Sambrotto et al., 1986). Between 2016 and 2019, the timing of the spring bloom peak varied between 25 April and 1 June and there were good agreements between estimates of the peak timing based on available estimates of GPP, NPP, NCP, and Chl-*a* standing stock biomass. Except for 2017, these years had no sea ice present in the southeastern Bering Sea at M2 (Stabeno & Bell, 2019). In the eastern Bering Sea the spring bloom timing has historically been linked to ice retreat, though the bloom may occur later when ice break up is early (before mid-March), or ice is nonexistent and prior to the cessation of winter storm events (Brown & Arrigo, 2013; Sigler et al., 2014). During the peak of the spring bloom in 2018 and 2019, rates for GPP were equivalent to $350\text{--}450 \text{ mg C m}^{-3} \text{ day}^{-1}$, NPP were equivalent to $200\text{--}250 \text{ mgC m}^{-3} \text{ day}^{-1}$, and NCP were equivalent to $100\text{--}150 \text{ mg C m}^{-3} \text{ day}^{-1}$. Primary production rates, calculated based on the estimated volumetric rates and integrated from surface to the mixed layer depth, were generally comparable to previously reported primary production estimates. For example, for 2016–2019, our spring integrated NPP estimates in May, which include the spring bloom period, ranged from $1,100$ to $1,900 \text{ mg C m}^{-2} \text{ day}^{-1}$ and are within previously reported ranges for discrete rates ($700\text{--}2,000 \text{ mg C m}^{-2} \text{ day}^{-1}$, Rho & Whitlege, 2007) and slightly higher than climatological estimates ($400\text{--}1,200 \text{ mg C m}^{-2} \text{ day}^{-1}$, Brown et al., 2011). Our NPP estimates of the period July–August ($\sim 270\text{--}790 \text{ mg C m}^{-2} \text{ day}^{-1}$), compared well to climatological average estimates for July–August ($\sim 500\text{--}750 \text{ mg C m}^{-2} \text{ day}^{-1}$) reported in (Brown et al., 2011), and discrete samples (Lomas et al., 2020, 2012). Overall, similar NPP values were reported for the Northern Bering Sea (Giesbrecht et al., 2019), though the range across years appears to be larger from 200 to $1,000 \text{ mg C m}^{-2} \text{ day}^{-1}$.

High water column integrated NCP rates during the peak bloom in both 2018 and 2019 highlight the importance the spring bloom has on community production of organic carbon. In the open ocean, at sufficiently large time and space scales, NCP is commonly assumed to be in approximate equilibrium with the downward export of carbon from the surface ocean (Brix et al., 2006). On the Bering Sea shelf, the fate of NCP appears more complex, with carbon exported laterally as well as vertically, and some accumulating in the biomass of higher trophic level organisms not captured by measures of POC or dissolved organic carbon (Baumann et al., 2013; Cross et al., 2014). At sub-seasonal scales, the relationship between NCP and vertical export flux will depend on how

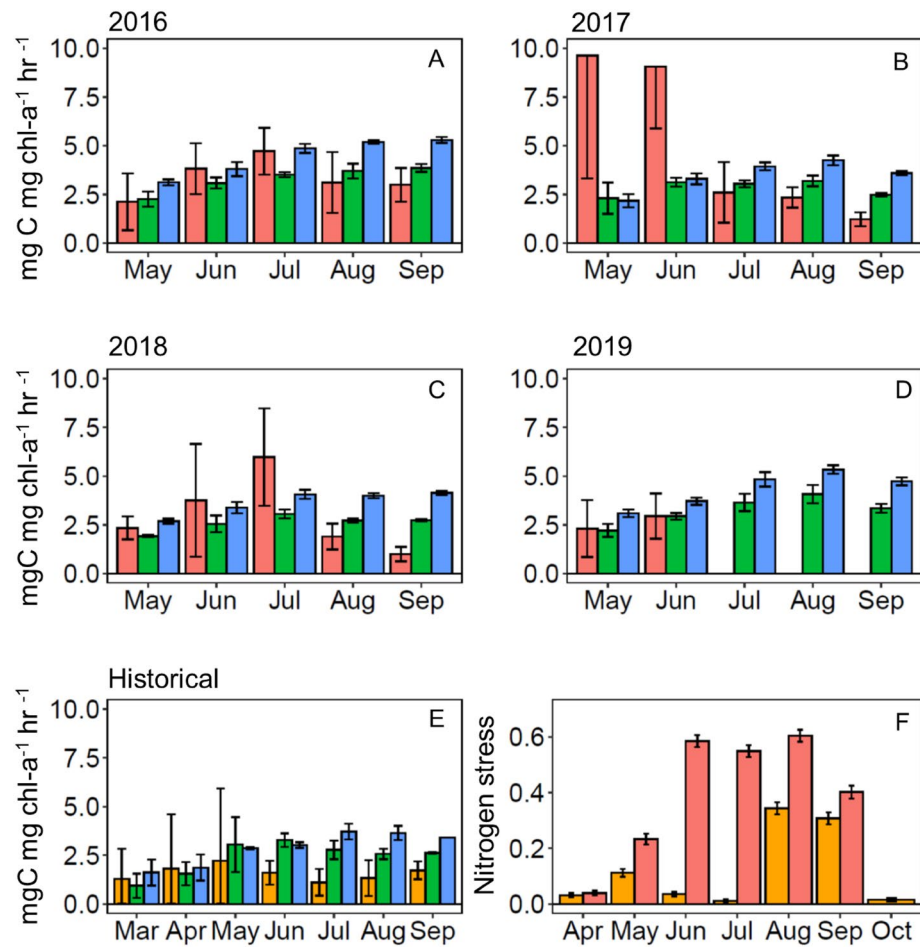


Figure 7. Barplots of average (\pm SD) photosynthetic capacity (p_{opt}^b , mg C mg Chl- a^{-1} hr $^{-1}$) for each month, based on Prawler GPP and chlorophyll- a (red), chlorophyll- a and temperature (green, Kameda & Ishizaka, 2005), temperature (blue, Behrenfeld & Falkowski, 1997) for (a) 2016, (b) 2017, (c) 2018, (d) 2019. (e) Historical in situ data for 2006–2019 in the southeastern Bering Sea, with orange colors being in situ production and Chl- a , p_{opt}^b estimates, and green and blue the Behrenfeld and Falkowski (1997) and Kameda and Ishizaka (2005) model derived p_{opt}^b values. (f) The apparent nutrient stress based on nitrogen (nitrate + ammonium) availability and nitrogen demand from Prawler (red), and discrete sample (orange) nitrogen production calculations from data measured on the southeastern Bering Sea middle shelf, ranging from 0 (no nitrogen stress) to 1 (full nitrogen stress).

organic carbon is partitioned between these various sinks, which may vary over time. Direct measurements of POC vertical fluxes suggest that 30%–50% of the carbon from primary producers can reach the benthos (Moran et al., 2012). Though as noted above, POC can also be transported across the shelf (Baumann et al., 2013), and evidence for respiration between the mixed layer and bottom in this study suggests that some of this flux may be reduced as it sinks. Our estimates of high carbon production associated with the spring bloom appear to occur during a span of 2–3 weeks. For carbon that does reach the seafloor, 50–121 mgC m $^{-2}$ day $^{-1}$ based upon bloom NPP and 30%–50% of NPP exported to the benthos, this “pulse” deposition is likely substantial enough to provide abundant dietary resources for benthic consumers, which may range from 35 to 221 mg C m $^{-2}$ day $^{-1}$ (Mordy et al., 2017; Rowe & Phoel, 1992). In addition, during the unusual year, 2017, the high phytoplankton biomass persisting below the mixed layer (~30–50 m deep or more) for 6–7 weeks after the spring bloom may also have been highly beneficial for grazing organisms.

Bloom NPP:GPP ratios were within the range of 0.5–0.9, in agreement with data from other coastal seas (Carvalho et al., 2017; Y. Huang et al., 2021; Spilling et al., 2019). NCP:GPP ratio estimates were as high as ~50% during the spring bloom period, values that align well with estimates based on POC data (Moran et al., 2012) and within the range of 0.2–0.6 as estimated previously (Prokopenko et al., 2011). As expected NCP:GPP ratios

were positively associated with higher standing stock Chl-*a* biomass (Eppley & Peterson, 1979), and followed an expected saturating function (K. Huang et al., 2012). Post bloom, we found low NCP:GPP ratios, and low or negative NCP rates indicating net heterotrophy. These results concur with previous analysis (Mordy et al., 2012), and suggest that after the bloom, carbon from primary producers is usually efficiently recycled in the upper ocean (Lomas et al., 2020). Overall, our analyses using daily to weekly data appeared to well capture the seasonal production cycle, and show that a large fraction of the primary production and potential resultant carbon export occurs in association with the spring bloom period.

4.3. Limited Phytoplankton Growth During Summer

Nutrient limitation directly reduces marine phytoplankton growth (Marañón et al., 2014) and previous in situ discrete data suggest nitrate limitation is a common occurrence in late summer on the shelves of the Bering (Lomas et al., 2012), and the Chukchi seas (Lewis et al., 2019). Our findings that phytoplankton growth capacity (p_{opt}^b) was low and that nutrient stress was probable in mid to late summer, indicate that primary production is primarily limited by nitrogen availability, rather than by temperature and irradiance levels during this time, consistent with previous observations (Lomas et al., 2012). Our nutrient stress calculations are based on measurements of apparent nitrate demand and availability. These calculations, also assume that nutrient recharge from deeper waters and recycling is not a major influencing factor, something that is probably a reasonable assumption for the M2 area in summer (Granger et al., 2013). It is well known that phytoplankton community compositions also shift as the ocean stratifies and nutrients are depleted in the surface layer during the growing season (Irwin et al., 2006). In the eastern Bering Sea, diatoms are abundant in spring and early summer, while dinoflagellates and smaller phytoplankton become more abundant later in the year (Moran et al., 2012). In addition, data from the Bering Sea also show that when nitrogen availability decreases, the relative fraction of smaller-sized picoplankton commonly increases (Eisner et al., 2016; Lomas et al., 2020). Such shifts in species composition influence community phytoplankton growth rates since the functional growth response to temperature in diatoms are almost three times that of dinoflagellates (Kremer et al., 2017). Cold water diatoms may respond even faster to enhanced temperature (Krause & Lomas, 2020). Smaller phytoplankton cells generally flourish in warmer and more stratified, low-nutrient waters (Irwin et al., 2006). Thus, the influence of nutrient limitation acts on both the individual phytoplankton species level as well as altering community growth rates (Kremer et al., 2017). Our results indicate that the apparent reductions in phytoplankton photosynthetic capacity ($p_{\text{opt}}^b < 2.5$) occurs during periods of higher probability of nutritional stress. In summer, these periods of lower p_{opt}^b and nutritional stress are a common and important feature of the production dynamics, and likely influences plankton size composition on the eastern Bering Sea shelf (Eisner et al., 2016; Lomas et al., 2020).

4.4. Improving Large-Scale Primary Production Estimates

Studies based on satellite ocean color data and discrete data, have suggested that NPP increases with warming temperatures in the Bering (Brown & Arrigo, 2013; Lomas et al., 2020) and Chukchi seas (Lewis et al., 2020). However, increasing phytoplankton production does not necessarily imply more production to fuel the ecosystem, particularly if warming also enhances the ratio of regenerated to new production, as suggested by nitrate uptake rates being lower during warm compared to cold years (Lomas et al., 2020). Our findings suggesting reduced phytoplankton production rates due to nitrogen limitation, highlight the need to develop ways to incorporate more realistic growth parameterizations for modeling primary production dynamics at larger scales on the Bering Sea shelf during summer, as has been noted elsewhere (Lee et al., 2015). Our comparisons were restricted to p_{opt}^b parameters used in global remotely sensed frameworks derived from temperature and Chl-*a* biomass (Kameda & Ishizaka, 2005) and temperature alone (Behrenfeld & Falkowski, 1997). Such approaches have been questioned in terms of the accuracy of the p_{opt}^b parameters (Regaudie-de-Gioux et al., 2014). Our analyses suggest that these global scaling relationships align well with the Prawler and discrete sample estimates of p_{opt}^b in spring and early summer. However, the low p_{opt}^b values, estimated from the Prawler and historical discrete sample data, commonly observed in late summer and early fall suggest that not accounting for apparent nutrient limitation in estimates of p_{opt}^b may result in systematic overestimation of summer primary production rates in the eastern Bering Sea. Pinpointing the onset of nutrient limited growth conditions, which vary inter-annually in terms of timing, could be done using mooring techniques as shown here, or from satellite techniques approximating nitrate concentrations (Goes et al., 2000). In addition, NPP frameworks that aim at incorporating nutrient limitation by including

dynamic carbon to Chl-*a* ratios (Silsbe et al., 2016; Westberry et al., 2008) may also better capture the reduced summer primary production dynamics. Alternatively, shifts in phytoplankton community size spectra observed using remote sensing algorithms (Brewin et al., 2011; Hirata et al., 2008; Waga et al., 2017) may provide an indication of overarching community compositional changes. This type of information would further allow adjustment of phytoplankton growth parameters based on community compositional information (Kremer et al., 2017; Lewis et al., 2019). Overall, the fusion of detailed process information from high temporal resolution, vertically resolved measurements of O₂ and Chl-*a* and improved large-scale production models (Y. Huang et al., 2021; Silsbe et al., 2016) will allow for better understanding of how the eastern Bering Sea shelf ecosystem will respond to ongoing climatic change.

Data Availability Statement

The in situ production data used here are available in Lomas et al. (2020). Prawler and weather data used for the analysis are available at https://data.pmel.noaa.gov/pmel/erddap/tabledap/ecofoci_prawler.html and https://data.pmel.noaa.gov/pmel/erddap/tabledap/weatherpak_m2.html. All other data use for the analyses in the paper are in Supporting Information S1.

Acknowledgments

The authors thank Geoff Lebon and Peter Proctor, for conducting the mooring and O₂ sampling, Deana Crouser for Chlorophyll-*a* analyses, the numerous field scientist that collected these data during the spring and fall 2016–2019, and Peggy Sullivan for help with data management. The authors thank Tom Cox for helpful clarifications concerning the GPP Fourier technique and are grateful for valuable comments from Jiaxu Zhang, Yibin Huang, and three anonymous reviewers that greatly improved the manuscript. This research was funded by two grants from the North Pacific Research Board (NPRB) Arctic Integrated Ecosystem Research Program AIERP: Arctic IES LTL (A92) and ASGARD, Phytoplankton Gap proposal (A961). The second award was to L.B.E. and M.W.L. and provided funding for a National Research Council fellowship to J.M.N. This publication is partially funded by the Cooperative Institute for Climate, Ocean, & Ecosystem Studies (CIOCES) under NOAA Cooperative Agreement NA20OAR4320271. NOAA/EcoFOCI maintains the M2 mooring and the Prawler, developed by the PMEL Innovative Technology for Arctic Exploration (ITAE) program and transitioned to EcoFOCI in 2021, is supported by NOAA PMEL. ITAE is a collaborative research effort by the University of Washington (CICOES) and NOAA engineers and scientists at PMEL and is funded by NOAA Research and PMEL. This is EcoFOCI contribution number EcoFOCI-1006, PMEL contribution number 5349 and CICOES contribution number 2021-1168.

References

- Baumann, M., Moran, S., Lomas, M., Kelly, R., & Bell, D. (2013). Seasonal decoupling of particulate organic carbon export and net primary production in relation to sea-ice at the shelf break of the eastern Bering Sea: Implications for off-shelf carbon export. *Journal of Geophysical Research: Oceans*, 118(10), 5504–5522. <https://doi.org/10.1002/jgrc.20366>
- Behrenfeld, M. J., & Falkowski, P. G. (1997). Photosynthetic rates derived from satellite-based chlorophyll concentration. *Limnology & Oceanography*, 42(1), 1–20. <https://doi.org/10.4319/lo.1997.42.1.0001>
- Bittig, H. C., Fiedler, B., Scholz, R., Krahnemann, G., & Körtzinger, A. (2014). Time response of oxygen optodes on profiling platforms and its dependence on flow speed and temperature. *Limnology and Oceanography: Methods*, 12(8), 617–636. <https://doi.org/10.4319/lom.2014.12.617>
- Bittig, H. C., Körtzinger, A., Neill, C., van Ooijen, E., Plant, J. N., Hahn, J., et al. (2018). Oxygen optode sensors: Principle, characterization, calibration, and application in the ocean. *Frontiers in Marine Science*, 4, 429. <https://doi.org/10.3389/fmars.2017.00429>
- Bouman, H. A., Platt, T., Doblin, M., Figueiras, F. G., Gudmundsson, K., Gudfinnsson, H. G., et al. (2018). Photosynthesis-irradiance parameters of marine phytoplankton: Synthesis of a global data set. *Earth System Science Data*, 10(1), 251–266. <https://doi.org/10.5194/essd-10-251-2018>
- Brewin, R. J., Hardman-Mountford, N. J., Lavender, S. J., Raitos, D. E., Hirata, T., Uitz, J., et al. (2011). An intercomparison of bio-optical techniques for detecting dominant phytoplankton size class from satellite remote sensing. *Remote Sensing of Environment*, 115(2), 325–339. <https://doi.org/10.1016/j.rse.2010.09.004>
- Brix, H., Gruber, N., Karl, D. M., & Bates, N. R. (2006). On the relationships between primary, net community, and export production in subtropical gyres. *Deep Sea Research Part II: Topical Studies in Oceanography*, 53(5–7), 698–717. <https://doi.org/10.1016/j.dsr2.2006.01.024>
- Brown, Z. W., & Arrigo, K. R. (2013). Sea ice impacts on spring bloom dynamics and net primary production in the Eastern Bering Sea. *Journal of Geophysical Research: Oceans*, 118(1), 43–62. <https://doi.org/10.1029/2012jc008034>
- Brown, Z. W., Van Dijken, G. L., & Arrigo, K. R. (2011). A reassessment of primary production and environmental change in the Bering Sea. *Journal of Geophysical Research: Oceans*, 116(C8), C08014. <https://doi.org/10.1029/2010jc006766>
- Carvalho, M. C., Schulz, K. G., & Eyre, B. D. (2017). Respiration of new and old carbon in the surface ocean: Implications for estimates of global oceanic gross primary productivity. *Global Biogeochemical Cycles*, 31(6), 975–984. <https://doi.org/10.1002/2016gb005583>
- Cassar, N., Wright, S. W., Thomson, P. G., Trull, T. W., Westwood, K. J., de Salas, M., et al. (2015). The relation of mixed-layer net community production to phytoplankton community composition in the Southern Ocean. *Global Biogeochemical Cycles*, 29(4), 446–462. <https://doi.org/10.1002/2014gb004936>
- Cheng, W., Curchitser, E., Stock, C., Hermann, A., Cokelet, E., Mordy, C., et al. (2016). What processes contribute to the spring and fall bloom co-variability on the Eastern Bering Sea shelf? *Deep Sea Research Part II: Topical Studies in Oceanography*, 134, 128–140. <https://doi.org/10.1016/j.dsr2.2015.07.009>
- Codispoti, L., Kelly, V., Thessen, A., Matrai, P., Suttles, S., Hill, V., et al. (2013). Synthesis of primary production in the Arctic Ocean: III. Nitrate and phosphate-based estimates of net community production. *Progress in Oceanography*, 110, 126–150. <https://doi.org/10.1016/j.pocean.2012.11.006>
- Copeman, L. A., Ryer, C. H., Eisner, L. B., Nielsen, J. M., Spencer, M. L., Iseri, P. J., & Ottmar, M. L. (2021). Decreased lipid storage in juvenile Bering Sea crabs (*Chionoecetes* spp.) in a warm (2014) compared to a cold (2012) year on the southeastern Bering Sea. *Polar Biology*, 44(9), 1–19. <https://doi.org/10.1007/s00300-021-02926-0>
- Cox, T. J. (2017). GPPFourier-An R package implementing the Fourier method to estimate Gross Primary Production from high-frequency O₂ data.
- Cox, T. J., Maris, T., Soetaert, K., Kromkamp, J. C., Meire, P., & Meysman, F. (2015). Estimating primary production from oxygen time series: A novel approach in the frequency domain. *Limnology and Oceanography: Methods*, 13(10), 529–552. <https://doi.org/10.1002/lom3.10046>
- Cox, T. J., van Beusekom, J. E., & Soetaert, K. (2017). Tune in on 11.57 μHz and listen to primary production. *Biogeosciences*, 14(22), 5271–5280. <https://doi.org/10.5194/bg-14-5271-2017>
- Coyle, K., & Gibson, G. (2017). Calanus on the Bering Sea shelf: Probable cause for population declines during warm years. *Journal of Plankton Research*, 39(2), 257–270. <https://doi.org/10.1093/plankt/fox005>
- Cronin, M. F., Pelland, N. A., Emerson, S. R., & Crawford, W. R. (2015). Estimating diffusivity from the mixed layer heat and salt balances in the North Pacific. *Journal of Geophysical Research: Oceans*, 120(11), 7346–7362. <https://doi.org/10.1002/2015jc011010>
- Cross, J. N., Mathis, J. T., Lomas, M. W., Moran, S. B., Baumann, M. S., Shull, D. H., et al. (2014). Integrated assessment of the carbon budget in the southeastern Bering Sea. *Deep Sea Research Part II: Topical Studies in Oceanography*, 109, 112–124. <https://doi.org/10.1016/j.dsr2.2014.03.003>

- Eisner, L. B., Gann, J. C., Ladd, C., Cieciel, K. D., & Mordy, C. W. (2016). Late summer/early fall phytoplankton biomass (chlorophyll *a*) in the eastern Bering Sea: Spatial and temporal variations and factors affecting chlorophyll-*a* concentrations. *Deep Sea Research Part II: Topical Studies in Oceanography*, *134*, 100–114. <https://doi.org/10.1016/j.dsr2.2015.07.012>
- Emerson, S., & Stump, C. (2010). Net biological oxygen production in the ocean—II: Remote in situ measurements of O₂ and N₂ in subarctic Pacific surface waters. *Deep Sea Research Part I: Oceanographic Research Papers*, *57*(10), 1255–1265. <https://doi.org/10.1016/j.dsr.2010.06.001>
- Emerson, S., Yang, B., White, M., & Cronin, M. (2019). Air-sea gas transfer: Determining bubble fluxes with in situ N₂ observations. *Journal of Geophysical Research: Oceans*, *124*(4), 2716–2727. <https://doi.org/10.1029/2018jc014786>
- Eppley, R. W., & Peterson, B. J. (1979). Particulate organic matter flux and planktonic new production in the deep ocean. *Nature*, *282*(5740), 677–680. <https://doi.org/10.1038/282677a0>
- Falkowski, P. G., Barber, R. T., & Smetacek, V. (1998). Biogeochemical controls and feedbacks on ocean primary production. *Science*, *281*(5374), 200–206. <https://doi.org/10.1126/science.281.5374.200>
- Freitas, F. H., White, A. E., & Quay, P. D. (2020). Diel measurements of oxygen-and carbon-based ocean metabolism across a trophic gradient in the North Pacific. *Global Biogeochemical Cycles*, *34*(11), e2019GB006518. <https://doi.org/10.1029/2019GB006518>
- Giesbrecht, K., Varela, D., Wiktor, J., Grebmeier, J., Kelly, B., & Long, J. (2019). A decade of summertime measurements of phytoplankton biomass, productivity, and assemblage composition in the Pacific Arctic Region from 2006 to 2016. *Deep Sea Research Part II: Topical Studies in Oceanography*, *162*, 93–113. <https://doi.org/10.1016/j.dsr2.2018.06.010>
- Goes, J. I., Saino, T., Oaku, H., Ishizaka, J., Wong, C. S., & Nojiri, Y. (2000). Basin scale estimates of sea surface nitrate and new production from remotely sensed sea surface temperature and chlorophyll. *Geophysical Research Letters*, *27*(9), 1263–1266. <https://doi.org/10.1029/1999gl002353>
- Granger, J., Prokopenko, M. G., Mordy, C. W., & Sigman, D. M. (2013). The proportion of remineralized nitrate on the ice-covered eastern Bering Sea shelf evidenced from the oxygen isotope ratio of nitrate. *Global Biogeochemical Cycles*, *27*(3), 962–971. <https://doi.org/10.1002/gbc.20075>
- Hansell, D. A., Whitley, T. E., & Goering, J. J. (1993). Patterns of nitrate utilization and new production over the Bering-Chukchi shelf. *Continental Shelf Research*, *13*(5–6), 601–627. [https://doi.org/10.1016/0278-4343\(93\)90096-g](https://doi.org/10.1016/0278-4343(93)90096-g)
- Hedges, J., Baldock, J., Gélinais, Y., Lee, C., Peterson, M., & Wakeham, S. (2002). The biochemical and elemental compositions of marine plankton: A NMR perspective. *Marine Chemistry*, *78*(1), 47–63. [https://doi.org/10.1016/s0304-4203\(02\)00009-9](https://doi.org/10.1016/s0304-4203(02)00009-9)
- Hersbach, H., Bell, B., Berrisford, P., Biavati, G., Horányi, A., Muñoz Sabater, J., et al. (2018). ERA5 hourly data on single levels from 1979 to present. In *Copernicus Climate Change Service (C3S) Climate Data Store (CDS)*.
- Hirata, T., Aiken, J., Hardman-Mountford, N., Smyth, T., & Barlow, R. (2008). An absorption model to determine phytoplankton size classes from satellite ocean color. *Remote Sensing of Environment*, *112*(6), 3153–3159. <https://doi.org/10.1016/j.rse.2008.03.011>
- Huang, K., Ducklow, H., Vernet, M., Cassar, N., & Bender, M. L. (2012). Export production and its regulating factors in the West Antarctica Peninsula region of the Southern Ocean. *Global Biogeochemical Cycles*, *26*(2). <https://doi.org/10.1029/2010GB004028>
- Huang, Y., Nicholson, D., Huang, B., & Cassar, N. (2021). Global estimates of marine gross primary production based on machine-learning upscaling of field observations. *Global Biogeochemical Cycles*, *35*, e2020GB006718. <https://doi.org/10.1029/2020GB006718>
- Hunt, G. L. J., Coyle, K. O., Eisner, L. B., Farley, E. V., Heintz, R. A., Mueter, F., et al. (2011). Climate impacts on eastern Bering Sea foodwebs: A synthesis of new data and an assessment of the Oscillating Control Hypothesis. *ICES Journal of Marine Science*, *68*(6), 1230–1243. <https://doi.org/10.1093/icesjms/fsr036>
- Irwin, A. J., Finkel, Z. V., Schofield, O. M., & Falkowski, P. G. (2006). Scaling-up from nutrient physiology to the size-structure of phytoplankton communities. *Journal of Plankton Research*, *28*(5), 459–471. <https://doi.org/10.1093/plankt/fbi148>
- Jerlov, N. G. (1976). *Marine optics*. Elsevier.
- Kameda, T., & Ishizaka, J. (2005). Size-fractionated primary production estimated by a two-phytoplankton community model applicable to ocean color remote sensing. *Journal of Oceanography*, *61*(4), 663–672. <https://doi.org/10.1007/s10872-005-0074-7>
- Kara, A. B., Rochford, P. A., & Hurlburt, H. E. (2000). Mixed layer depth variability and barrier layer formation over the North Pacific Ocean. *Journal of Geophysical Research: Oceans*, *105*(C7), 16783–16801. <https://doi.org/10.1029/2000jc900071>
- Kimmel, D. G., Eisner, L. B., Wilson, M. T., & Duffy-Anderson, J. T. (2018). Copepod dynamics across warm and cold periods in the eastern Bering Sea: Implications for walleye pollock (*Gadus chalcogrammus*) and the Oscillating Control Hypothesis. *Fisheries Oceanography*, *27*(2), 143–158. <https://doi.org/10.1111/fog.12241>
- Krause, J. W., & Lomas, M. W. (2020). Understanding diatoms' past and future biogeochemical role in high-latitude seas. *Geophysical Research Letters*, *47*(1), e2019GL085602. <https://doi.org/10.1029/2019gl085602>
- Kremer, C. T., Thomas, M. K., & Litchman, E. (2017). Temperature-and size-scaling of phytoplankton population growth rates: Reconciling the Eppley curve and the metabolic theory of ecology. *Limnology & Oceanography*, *62*(4), 1658–1670. <https://doi.org/10.1002/lno.10523>
- Ladd, C., & Staben, P. J. (2012). Stratification on the eastern Bering Sea shelf revisited. *Deep Sea Research Part II: Topical Studies in Oceanography*, *65–70*, 72–83. <https://doi.org/10.1016/j.dsr2.2012.02.009>
- Laws, E. A. (1991). Photosynthetic quotients, new production, and net community production in the open ocean. *Deep-Sea Research, Part A: Oceanographic Research Papers*, *38*(1), 143–167. [https://doi.org/10.1016/0198-0149\(91\)90059-o](https://doi.org/10.1016/0198-0149(91)90059-o)
- Lee, Y. J., Matrai, P. A., Friedrichs, M. A. M., Saba, V. S., Antoine, D., Ardyna, M., et al. (2015). An assessment of phytoplankton primary productivity in the Arctic Ocean from satellite ocean color/in situ chlorophyll-*a* based models. *Journal of Geophysical Research: Oceans*, *120*(9), 6508–6541. <https://doi.org/10.1002/2015JC011018>
- Lewis, K., Arntsen, A., Coupel, P., Joy-Warren, H., Lowry, K., Matsuoka, A., et al. (2019). Photoacclimation of Arctic Ocean phytoplankton to shifting light and nutrient limitation. *Limnology & Oceanography*, *64*(1), 284–301. <https://doi.org/10.1002/lno.11039>
- Lewis, K., Van Dijken, G., & Arrigo, K. R. (2020). Changes in phytoplankton concentration now drive increased Arctic Ocean primary production. *Science*, *369*(6500), 198–202. <https://doi.org/10.1126/science.aay8380>
- Liang, J. H., Deutsch, C., McWilliams, J. C., Baschek, B., Sullivan, P. P., & Chiba, D. (2013). Parameterizing bubble-mediated air-sea gas exchange and its effect on ocean ventilation. *Global Biogeochemical Cycles*, *27*(3), 894–905. <https://doi.org/10.1002/gbc.20080>
- Lomas, M. W., Eisner, L. B., Gann, J., Baer, S. E., Mordy, C. W., & Staben, P. J. (2020). Time-series of direct primary production and phytoplankton biomass in the southeastern Bering Sea: Responses to cold and warm stanzas. *Marine Ecology Progress Series*, *642*, 39–54. <https://doi.org/10.3354/meps13317>
- Lomas, M. W., Moran, S. B., Casey, J. R., Bell, D. W., Tiablo, M., Whitefield, J., et al. (2012). Spatial and seasonal variability of primary production on the eastern Bering Sea shelf. *Deep Sea Research Part II: Topical Studies in Oceanography*, *65–70*, 126–140. <https://doi.org/10.1016/j.dsr2.2012.02.010>

- Marañón, E., Cermeño, P., Huete-Ortega, M., López-Sandoval, D. C., Mouriño-Carballido, B., & Rodríguez-Ramos, T. (2014). Resource supply overrides temperature as a controlling factor of marine phytoplankton growth. *PLoS One*, 9(6), e99312. <https://doi.org/10.1371/journal.pone.0099312>
- Mesa, E., Delgado-Huertas, A., Carrillo-de-Albornoz, P., García-Corral, L. S., Sanz-Martín, M., Wassmann, P., et al. (2017). Continuous daylight in the high-Arctic summer supports high plankton respiration rates compared to those supported in the dark. *Scientific Reports*, 7(1), 1247. <https://doi.org/10.1038/s41598-017-01203-7>
- Moore, C., Mills, M., Arrigo, K., Berman-Frank, I., Bopp, L., Boyd, P., et al. (2013). Processes and patterns of oceanic nutrient limitation. *Nature Geoscience*, 6(9), 701–710. <https://doi.org/10.1038/ngeo1765>
- Moran, S., Lomas, M., Kelly, R., Gradinger, R., Iken, K., & Mathis, J. (2012). Seasonal succession of net primary productivity, particulate organic carbon export, and autotrophic community composition in the eastern Bering Sea. *Deep Sea Research Part II: Topical Studies in Oceanography*, 65, 84–97. <https://doi.org/10.1016/j.dsr2.2012.02.011>
- Mordy, C. W., Cokelet, E. D., Ladd, C., Menzia, F. A., Proctor, P., Stabeno, P. J., & Wisegarver, E. (2012). Net community production on the middle shelf of the eastern Bering Sea. *Deep Sea Research Part II: Topical Studies in Oceanography*, 65–70, 110–125. <https://doi.org/10.1016/j.dsr2.2012.02.012>
- Mordy, C. W., Devol, A., Eisner, L. B., Kachel, N., Ladd, C., Lomas, M. W., et al. (2017). Nutrient and phytoplankton dynamics on the inner shelf of the eastern Bering Sea. *Journal of Geophysical Research: Oceans*, 122(3), 2422–2440. <https://doi.org/10.1002/2016JC012071>
- Mordy, C. W., Eisner, L., Kearney, K., Kimmel, D., Lomas, M. W., Mier, K., et al. (2021). Spatiotemporal variability of the nitrogen deficit in bottom waters on the eastern Bering Sea shelf. *Continental Shelf Research*, 224, 104423. <https://doi.org/10.1016/j.csr.2021.104423>
- NOAA/PMEL EcoFOCI. M2 mooring surface weather data in the southeast Bering Sea for 2016–2019 [Dataset]. https://data.pmel.noaa.gov/pmel/erddap/tabledap/weatherpak_m2.html
- NOAA/PMEL EcoFOCI. Prowler in situ data at M2 mooring location from a moored profiling instrument in the southeast Bering Sea for 2016–2019 [Dataset]. https://data.pmel.noaa.gov/pmel/erddap/tabledap/ecofoci_prowler.html
- Osse, T. J., Meinig, C., Stalin, S., & Milburn, H. (2015). The PRAWLER, a vertical profiler powered by wave energy. In *Paper presented at OCEANS 2015-MTS/IEEE Washington*. IEEE.
- Parsons, T. R. (1984). *A manual of chemical and biological methods for seawater analysis*. Elsevier.
- Pelland, N. A., Eriksen, C. C., Emerson, S. R., & Cronin, M. F. (2018). Seaglider surveys at ocean station Papa: Oxygen kinematics and upper-ocean metabolism. *Journal of Geophysical Research: Oceans*, 123(9), 6408–6427. <https://doi.org/10.1029/2018JC014091>
- Platt, T., Harrison, W. G., Horne, E. P., & Irwin, B. (1987). Carbon fixation and oxygen evolution by phytoplankton in the Canadian High Arctic. *Polar Biology*, 8(2), 103–113. <https://doi.org/10.1007/bf00297064>
- Prokopenko, M. G., Pauluis, O. M., Granger, J., & Yeung, L. Y. (2011). Exact evaluation of gross photosynthetic production from the oxygen triple-isotope composition of O₂: Implications for the net-to-gross primary production ratios. *Geophysical Research Letters*, 38(14). <https://doi.org/10.1029/2011gl047652>
- R Core Team. (2018). *R: A language and environment for statistical computing*. R Foundation for Statistical Computing. Retrieved from <http://r-project.org>
- Regaudie-de-Gioux, A., & Duarte, C. M. (2012). Temperature dependence of planktonic metabolism in the ocean. *Global Biogeochemical Cycles*, 26(1). <https://doi.org/10.1029/2010gb003907>
- Regaudie-de-Gioux, A., & Duarte, C. M. (2013). Global patterns in oceanic planktonic metabolism. *Limnology & Oceanography*, 58(3), 977–986. <https://doi.org/10.4319/lo.2013.58.3.0977>
- Regaudie-de-Gioux, A., Lasternas, S., Agustí, S., & Duarte, C. M. (2014). Comparing marine primary production estimates through different methods and development of conversion equations. *Frontiers in Marine Science*, 1, 19. <https://doi.org/10.3389/fmars.2014.00019>
- Rho, T., & Whitledge, T. E. (2007). Characteristics of seasonal and spatial variations of primary production over the southeastern Bering Sea shelf. *Continental Shelf Research*, 27(20), 2556–2569. <https://doi.org/10.1016/j.csr.2007.07.006>
- Rowe, G. T., & Phoel, W. C. (1992). Nutrient regeneration and oxygen demand in Bering Sea continental shelf sediments. *Continental Shelf Research*, 12(4), 439–449. [https://doi.org/10.1016/0278-4343\(92\)90085-x](https://doi.org/10.1016/0278-4343(92)90085-x)
- Sambrotto, R. N., Mordy, C., Zeeman, S. I., Stabeno, P. J., & Macklin, S. A. (2008). Physical forcing and nutrient conditions associated with patterns of Chl *a* and phytoplankton productivity in the southeastern Bering Sea during summer. *Deep Sea Research Part II: Topical Studies in Oceanography*, 55(16–17), 1745–1760. <https://doi.org/10.1016/j.dsr2.2008.03.003>
- Sambrotto, R. N., Niebauer, H., Goering, J., & Iverson, R. (1986). Relationships among vertical mixing, nitrate uptake, and phytoplankton growth during the spring bloom in the southeast Bering Sea middle shelf. *Continental Shelf Research*, 5(1–2), 161–198. [https://doi.org/10.1016/0278-4343\(86\)90014-2](https://doi.org/10.1016/0278-4343(86)90014-2)
- Sigler, M. F., Napp, J. M., Stabeno, P. J., Heintz, R. A., Lomas, M. W., & Hunt, G. L., Jr. (2016). Variation in annual production of copepods, euphausiids, and juvenile walleye pollock in the southeastern Bering Sea. *Deep Sea Research Part II: Topical Studies in Oceanography*, 134, 223–234. <https://doi.org/10.1016/j.dsr2.2016.01.003>
- Sigler, M. F., Stabeno, P. J., Eisner, L. B., Napp, J. M., & Mueter, F. J. (2014). Spring and fall phytoplankton blooms in a productive subarctic ecosystem, the eastern Bering Sea, during 1995–2011. *Deep Sea Research Part II: Topical Studies in Oceanography*, 109, 71–83. <https://doi.org/10.1016/j.dsr2.2013.12.007>
- Silsbe, G. M., Behrenfeld, M. J., Halsey, K. H., Milligan, A. J., & Westberry, T. K. (2016). The CAFE model: A net production model for global ocean phytoplankton. *Global Biogeochemical Cycles*, 30(12), 1756–1777. <https://doi.org/10.1002/2016gb005521>
- Spilling, K., Fuentes-Lema, A., Quemaliños, D., Klais, R., & Sobrino, C. (2019). Primary production, carbon release, and respiration during spring bloom in the Baltic Sea. *Limnology & Oceanography*, 64(4), 1779–1789. <https://doi.org/10.1002/lno.11150>
- Springer, A. M., McRoy, C. P., & Flint, M. V. (1996). The Bering Sea Green Belt: Shelf-edge processes and ecosystem production. *Fisheries Oceanography*, 5(3–4), 205–223. <https://doi.org/10.1111/j.1365-2419.1996.tb00118.x>
- Stabeno, P. J., & Bell, S. W. (2019). Extreme conditions in the Bering Sea (2017–2018): Record-breaking low sea-ice extent. *Geophysical Research Letters*, 46(15), 8952–8959. <https://doi.org/10.1029/2019gl083816>
- Stabeno, P. J., Bond, N., Kachel, N., Salo, S., & Schumacher, J. (2001). On the temporal variability of the physical environment over the south-eastern Bering Sea. *Fisheries Oceanography*, 10(1), 81–98. <https://doi.org/10.1046/j.1365-2419.2001.001157.x>
- Stabeno, P. J., Bond, N., & Salo, S. (2007). On the recent warming of the southeastern Bering Sea shelf. *Deep Sea Research Part II: Topical Studies in Oceanography*, 54(23–26), 2599–2618. <https://doi.org/10.1016/j.dsr2.2007.08.023>
- Stabeno, P. J., Napp, J., Mordy, C., & Whitledge, T. (2010). Factors influencing physical structure and lower trophic levels of the eastern Bering Sea shelf in 2005: Sea ice, tides, and winds. *Progress in Oceanography*, 85(3–4), 180–196. <https://doi.org/10.1016/j.pocean.2010.02.010>
- Staehr, P. A., Testa, J. M., Kemp, W. M., Cole, J. J., Sand-Jensen, K., & Smith, S. V. (2012). The metabolism of aquatic ecosystems: History, applications, and future challenges. *Aquatic Sciences*, 74(1), 15–29. <https://doi.org/10.1007/s00027-011-0199-2>

- Stanley, R. H., Kirkpatrick, J. B., Cassar, N., Barnett, B. A., & Bender, M. L. (2010). Net community production and gross primary production rates in the western equatorial Pacific. *Global Biogeochemical Cycles*, *24*(4). <https://doi.org/10.1029/2009gb003651>
- Stoecker, D. K., Weigel, A. C., Stockwell, D. A., & Lomas, M. W. (2014). Microzooplankton: Abundance, biomass, and contribution to chlorophyll in the eastern Bering Sea in summer. *Deep Sea Research Part II: Topical Studies in Oceanography*, *109*, 134–144. <https://doi.org/10.1016/j.dsr2.2013.09.007>
- Sun, O. M., Jayne, S. R., Polzin, K. L., Rahter, B. A., & Laurent, L. C. S. (2013). Scaling turbulent dissipation in the transition layer. *Journal of Physical Oceanography*, *43*(11), 2475–2489. <https://doi.org/10.1175/jpo-d-13-057.1>
- Uitz, J. U., Huot, Y., Bruyant, F., Babin, M., & Claustre, H. (2008). Relating phytoplankton photophysiological properties to community structure on large scales. *Limnology & Oceanography*, *53*(2), 614–630. <https://doi.org/10.4319/lo.2008.53.2.0614>
- Waga, H., Hirawake, T., Fujiwara, A., Kikuchi, T., Nishino, S., Suzuki, K., et al. (2017). Differences in rate and direction of shifts between phytoplankton size structure and sea surface temperature. *Remote Sensing*, *9*(3), 222. <https://doi.org/10.3390/rs9030222>
- Westberry, T., Behrenfeld, M., Siegel, D., & Boss, E. (2008). Carbon-based primary productivity modeling with vertically resolved photoacclimation. *Global Biogeochemical Cycles*, *22*(2). <https://doi.org/10.1029/2007gb003078>